RSC Mechanochemistry

ROYAL SOCIETY OF CHEMISTRY

PAPER

View Article Online
View Journal | View Issue

Cite this: *RSC Mechanochem.*, 2025, **2**, 706

Mechanism of plasmon-driven molecular jackhammers in mechanical opening and disassembly of membranes†

Ciceron Ayala-Orozco, *[ae] Vardan Vardanyan,[a] Katherine Lopez-Jaime,[b] Zicheng Wang,[a] Jorge M. Seminario, *[bc] Anatoly B. Kolomeisky *[a] and James M. Tour *[ad]

Plasmon-driven molecular jackhammers (MJHs) are a type of molecular machine that converts photon energy into mechanical energy. Upon insertion into lipid bilayers followed by near-infrared light activation, plasmon-driven MJH mechanically open cellular membranes through a process that is not inhibited by reactive oxygen species (ROS) inhibitors and does not induce thermal heating. The molecular mechanism by which the plasmon-driven MJH open and disassemble cellular membranes has not hitherto been established. Herein, we differentiate the mechanical mechanism in MJHs from the ROS-mediated chemical effects in photodynamic therapy or thermal effects in photothermal therapy. We further present a detailed molecular mechanism for the plasmon-driven MJH disassembly of lipid bilayers. The mechanical studies on plasmon-driven MJH disassembly processes on artificial lipid bilayers were done using ROS-unreactive saturated phytanoyl phospholipids. We were able to capture in real-time the lipid bilayer disassembly by MJHs using fluorescence confocal microscopy on saturated phospholipids in giant unilamellar vesicles.

Received 29th July 2024
Accepted 8th June 2025

DOI: 10.1039/d4mr00083h

rsc.li/RSCMechanochem

Introduction

Plasmons are the collective oscillation of conduction band electrons in materials upon their excitation with electromagnetic radiation, specifically photons.[1] The strong electromagnetic field enhancement in optical plasmonic materials has been exploited for a wide range of applications, including optoelectronic devices, sensors, ultrasensitive analyte detection, cancer theranostics, solar energy harvesting, water desalination, and photocatalysis.[2–14] Most of the research in optical plasmons have been conducted on nanomaterials.[15–17] Plasmons in small organic molecules have been theoretically proposed, and they have recently been investigated experimentally in ideal polycyclic aromatic hydrocarbons.[18–22] We recently showed that cyanine dyes act as plasmon-driven molecular jackhammers (MJHs) through vibronic (electronic + vibrational) mode activation that causes the molecule to stretch longitudinally and axially through concerted whole-molecule vibrations.[23,24] Cyanine dyes support intrinsic molecular plasmon resonances upon near-infrared (NIR) light excitation that induces the concerted whole-molecule vibrational motion, enabling conversion of photon energy to mechanical energy.[23,24] In this process, the plasmon-driven action is coupled with the concerted whole-molecule vibration in MJHs, also known as vibronic-driven action (VDA).[23] Others have established that the vibrational energy transfer is fundamentally a mechanical process discovered by studying molecules with vibrational lifetimes with unexpected inverse temperature dependence.[25–27] This means that the vibrational energy transfer does not necessarily increase the temperature of the solvent since it was found to be fundamentally a mechanical process.[25,27] Here, similarly, the whole-molecule vibrational motion in MJHs is a vibrational energy transfer process, which fundamentally is a mechanical action that does not itself induce an increase in the temperature of the media. It is also unaffected by cooling the media to 2 °C.[23] Moreover, others have independently demonstrated that this type of whole-molecule vibration is a mechanical action and not simply a thermal heating process, in agreement with our evidence in MJHs.[28,29]

[a]*Department of Chemistry, Rice University, Houston, Texas 77005, USA. E-mail: ciceron.orozco@gmail.com; tour@rice.edu; tolya@rice.edu*

[b]*Department of Chemical Engineering and Department of Electrical and Computer Engineering, Texas A&M University, College Station, Texas, 77843, USA. E-mail: seminario@tamu.edu*

[c]*Department of Materials Science and Engineering, Texas A&M University, College Station, Texas, 77843, USA*

[d]*Department of Materials Science and NanoEngineering, The NanoCarbon Center, The Smalley-Curl Institute and the Rice Advanced Materials Institute, Rice University, Houston, Texas 77005, USA*

[e]*The Molecular Jackhammer Cancer Therapeutics Institute, Houston, Texas 77230, USA*

† Electronic supplementary information (ESI) available: Additional spectra, graphs, flow cytometry analyses and figures. See DOI: https://doi.org/10.1039/d4mr00083h

Upon insertion into lipid bilayers followed by NIR light activation, plasmon-driven MJHs mechanically open cellular membranes enabling eradication of cancer cells in culture and tumors in mice.[23] A photothermal mechanism cannot explain the membrane-opening activity, as photothermal effects are directly proportional to both the optical molar extinction and the concentration of the molecule.[30] To differentiate mechanical effects from photothermal effects, we conducted experiments at low concentrations (4 μM or lower), where the thermal effects were negligible.[23] Further evidence was obtained by comparing two molecules at the same concentration (2.7 μM): a strong MJH Cy7.5-amine *versus* a weak MJH Cy7-amine. Although the weak MJH Cy7-amine has a higher molar extinction than Cy7.5-amine, it was significantly less effective at opening cell membranes.[23,31] A similar trend was observed when comparing the strong MJH Cy5.5-amine with the weak MJH Cy5-amine. Comparisons show that a more active molecule (a stronger MJH) possesses a higher plasmonicity index, which correlates with whole-molecule vibrations in cyanines. Additionally, the molecule with the highest activity, BL-204, has one of the lowest extinction values in a comparative study of 24 cyanine molecules.[31] We found that even lower concentrations (0.12 μM) were sufficient for the most active MJH to open cell membranes, where photothermal effects are negligible. The highest plasmonicity of BL-204, compared to the other 23 molecules studied, explains its superior MJH potency.[24,31] Furthermore, it is important to consider the small structural differences between Cy7-amine and Cy7.5-amine to better understand the local thermal effects within the membrane. In the experiments, the molecular structure was kept constant using Cy7-amine. The whole-molecule vibration of Cy-7-amine was excited with 680 nm light, and it was compared to excitation with 730 nm light, which primarily promotes longitudinal vibrations along the polymethine chain in the cyanine.[23,24] It is expected that more localized heat would be deposited with the higher photon absorption at 730 nm due to its greater molar extinction compared to 680 nm excitation. However, the results indicated that a higher level of membrane permeabilization activity was observed with the 680 nm excitation.[23] Collectively, these experiments suggest that thermal effects are not the primary factor responsible for opening cell membranes in MJHs.

It is possible that photodynamic ROS effects are responsible for opening the cell membranes or that the permeabilization of cellular membranes is a consequence of rapid cell death, and not as a result of direct mechanical action on lipid membranes. Here, we rule out both ROS and rapid cell death as reasons for the massive cell membrane disruption. This is done by studying the plasmon-driven MJH mechanical effects using fully synthetic and oxidation-resistant lipid bilayers. This was shown in one case in our previous study,[23] but here more cases are analyzed comprehensively with additional evidence that strongly supports the mechanical mechanism. The evidence suggests that cell-death mediated mechanisms and ROS reactivity can only cause opening of the lipid bilayers in living cells at relatively high concentrations of ROS with long exposure times, and ROS causes slow cell death through oxidative stress. We use artificial and organelle-free giant unilamellar vesicles (GUVs) that were synthesized with ROS-unreactive saturated 1,2-diphytanoyl-*sn*-glycero-3-phosphocholine (DPhPC) phospholipids.

Phytanoyl lipids in the cell membranes of extremophilic *Archaea* help the organism to survive harsh habitats at high temperatures and to endure high salt or acid concentrations.[32] Their chemical stability is attributed to the saturated alkyl chains, which are much less sensitive to chemical oxidation than unsaturated alkyl chains.[32] DPhPC is a synthetic ester lipid with methylated tails. DPhPC was originally synthesized to form oxidation-resistant, stable lipid bilayers for *in vitro* experiments with artificial membranes.[33] DPhPC lipid bilayers possess high chemical, mechanical and thermal stability and do not leak ions in the absence of a pore or ion channel. The bilayers show no phase transitions over a broad range of temperatures from −120 °C to +120 °C.[34]

ROS-mediated lipid membrane disruption in unsaturated lipids has been investigated.[35–38] The expansion of the lipid vesicles is a major characteristic of the ROS-mediated disruption of lipid vesicles due to the reaction of singlet oxygen with carbon–carbon double bonds or allylic protons in the unsaturated phospholipids.[35,37,39] In contrast, here, we show that the mechanically mediated opening and disassembly of DPhPC lipid bilayers cause shrinkage, not the ROS-mediated-like expansion of the GUV, likely due to the stepwise mechanical ejection of phospholipids followed by a hole-closing reassembly process. This leads to successive shrinking of the GUV diameter until final collapse upon reaching a critical minimal size. Similarly, we detected live cell membrane permeabilization and shrinking when the cells were subjected to the mechanical effects of plasmon-driven MJHs. Flow cytometry analysis is further evidence that the cell membrane permeabilization occurs through mechanical action by plasmon-driven MJHs and not by a thermal effect.

Numerous strategies have been explored for the opening and release of cargo from lipid vesicles and liposomes.[40–43] However, especially for light-activated strategies, it is essential to thoroughly understand the underlying mechanisms for designing more effective molecular agents. Often, assumptions about these mechanisms are made without fully evaluating and accounting for the contributions of thermal, photodynamic, or mechanical effects. These different mechanisms can sometimes have opposing impacts, and a misunderstanding of how they interact might lead to ineffective new designs. In this study, we systematically investigate all of these effects and provide definitive insights into the mechanism of action of light-activated MJHs.

Results and discussion

Cyanine Cy5.5 is a plasmon-driven MJH

Cyanine dyes, particularly Cy5.5, support longitudinal molecular plasmons (LMPs) and transversal molecular plasmons (TMPs) as shown in Fig. 1A.[23] Note that there is a positive charge on the nitrogen in the benzoindole structure, as illustrated in Fig. 1A. The induced charge density of the molecular plasmon

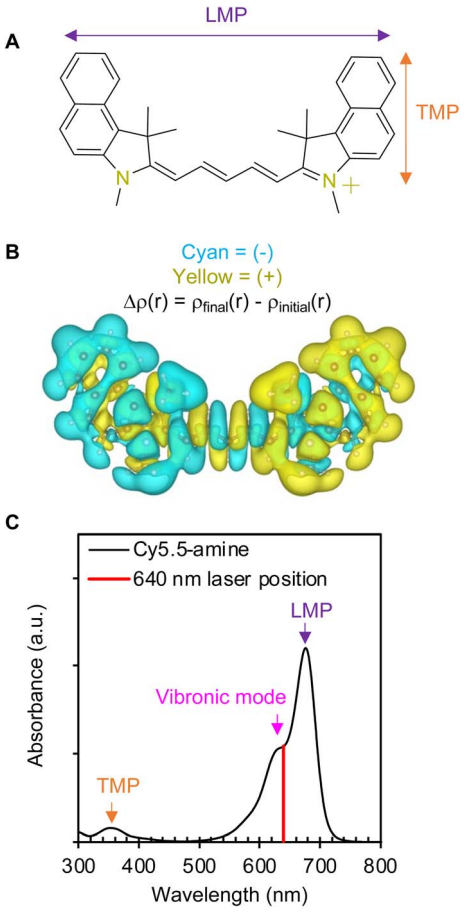

Fig. 1 Cyanine Cy5.5 is a molecular plasmon. (A) The chemical structure of cyanine Cy5.5. The horizontal arrow (teal) indicates the orientation of the longitudinal molecular plasmon (LMP) and the vertical arrow (orange) indicates the orientation of the transversal molecular plasmon (TMP). (B) Calculated induced charge density of the molecular plasmon using time-dependent density-functional theory (TD-DFT). The electric field is used to simulate the optical excitation of Cy5.5. The total induced charge density [$\Delta\rho(r)$] is calculated at 640 nm wavelength. Cyan color represents induced negative charge density (–). Yellow color represents induced positive charge density (+). (C) The experimental absorption spectrum of Cy5.5-amine showing the absorption positions of the LMP and TMP. The long alkyl-amine arm in the Cy5.5-amine structure (Fig. 2) was not included in the TD-DFT calculation because it has negligible contributions to the conjugation of the core structure. Instead, a methyl group was substituted for the long alkyl-amine in Cy5.5-amine. The red line represents the laser excitation wavelength.

in Cy5.5 was calculated using time-dependent density functional theory (TD-DFT) that is shown in Fig. 1B. The electric field was used to simulate the optical excitation of Cy5.5, and the total induced charge density [$\Delta\rho(r)$] was calculated at 640 nm wavelength. This induced charge density in Cy5.5 is a characteristic electronic charge oscillation of molecular plasmons in cyanines.[23] The LMPs and TMPs were assigned in the absorption spectrum of Cy5.5-amine, as shown in Fig. 1C. When a molecular plasmon mode is photoactivated, the electronic and vibrational oscillations are coupled in a vibronic mode. We have previously established that cyanine dyes act as plasmon-driven MJHs through vibronic mode activation that causes the molecule to stretch longitudinally and axially, leading to a concerted whole-molecule vibration.[23,24] This process enables the conversion of photon energy to mechanical energy, analogous to a "molecular breathing mode" that is estimated to be in the order of 40×10^{12} oscillations s^{-1} (40 THz).[24,31] In this study, we accomplished the vibronic mode activation using a 640 nm laser (Fig. 1C) or 630 nm LED light (Fig. S1 of the ESI†). The purpose of the TD-DFT calculation here is to conceptualize the molecular plasmons in Cy5.5-amine. A comprehensive theoretical description of the molecular plasmons and their respective vibrational modes in a cyanine dye (Cy7.5-amine) can be found in our former studies.[23,24,31]

The molecular mechanism for plasmon-driven MJH disassembly in synthetic lipid vesicles

The artificial GUVs used in this study were synthesized utilizing DPhPC phospholipids, as shown in Fig. 2A. These phospholipids introduce oxidation-resistant and thermal stability in synthetic lipid vesicles due to their fully saturated and methylated alkyl chains. The MJH Cy5.5-amine is shown in Fig. 2A. The Cy5.5-amine interacts with the polar head in DPhPC, as shown in Fig. 2A; this mode of binding was validated by molecular dynamics simulation (Fig. 2B). The less polar portion of the MJH, the pentamethine bridge connected to benzoindole, is inserted into the lipid bilayer (Fig. 2B). This is applicable in both: (1) a DPhPC membrane with zwitterionic phosphocholine head groups and fully saturated alkyl tails and (2) a charged (1-palmitoyl-2-oleoyl-*glycero*-3-phosphocholine/1-palmitoyl-2-oleoyl-*sn*-glycero-3-phosphoethanolamine/1-palmitoyl-2-oleoyl-*sn*-glycero-3-phospho-(1′-rac-glycerol)) (POPC/POPE/POPG) membrane with 6% content of negatively charged phosphoglycerol and unsaturated alkyl tails (see ESI Fig. S2†). In addition, Cy5.5-amine with an initial position outside the DPhPC membrane in the simulation was able to interact and insert in the lipid bilayer, further confirming this mode of biding (see ESI Fig. S3†). The light activation of plasmon-driven MJHs induces mechanical force in the form of ultrafast vibrational motion that is transferred to the adjacent DPhPC lipids. This whole-molecule vibrational mode was measured by Raman spectroscopy, and the mechanical force exerted on the lipid bilayer was estimated below. Subsequently, the lipids are ejected outside the lipid vesicle (Fig. 2C), as suggested by the experimental results. This lipid ejection creates vacancies in the lipid bilayer. A self-assembling process that is driven by hydrophobic interactions leads to reassembly of the lipids to close the vacancies in the bilayer, resulting in a lipid vesicle of reduced size, as shown in Fig. 2D. These steps can be repeated until the lipid vesicle reaches a critical minimal size where it collapses. The disordered lipids that were forced to the inside of the vesicle further promote the collapse of the lipid vesicle when a critical size is reached. This proposed molecular mechanism is consistent with the experimental observations in Fig. 3.

Unlike cavitation, where bubbles form, expand, and then collapse,[44] our observations show that there is no expansion of the vesicles or formation of bubbles. In our measurements, we

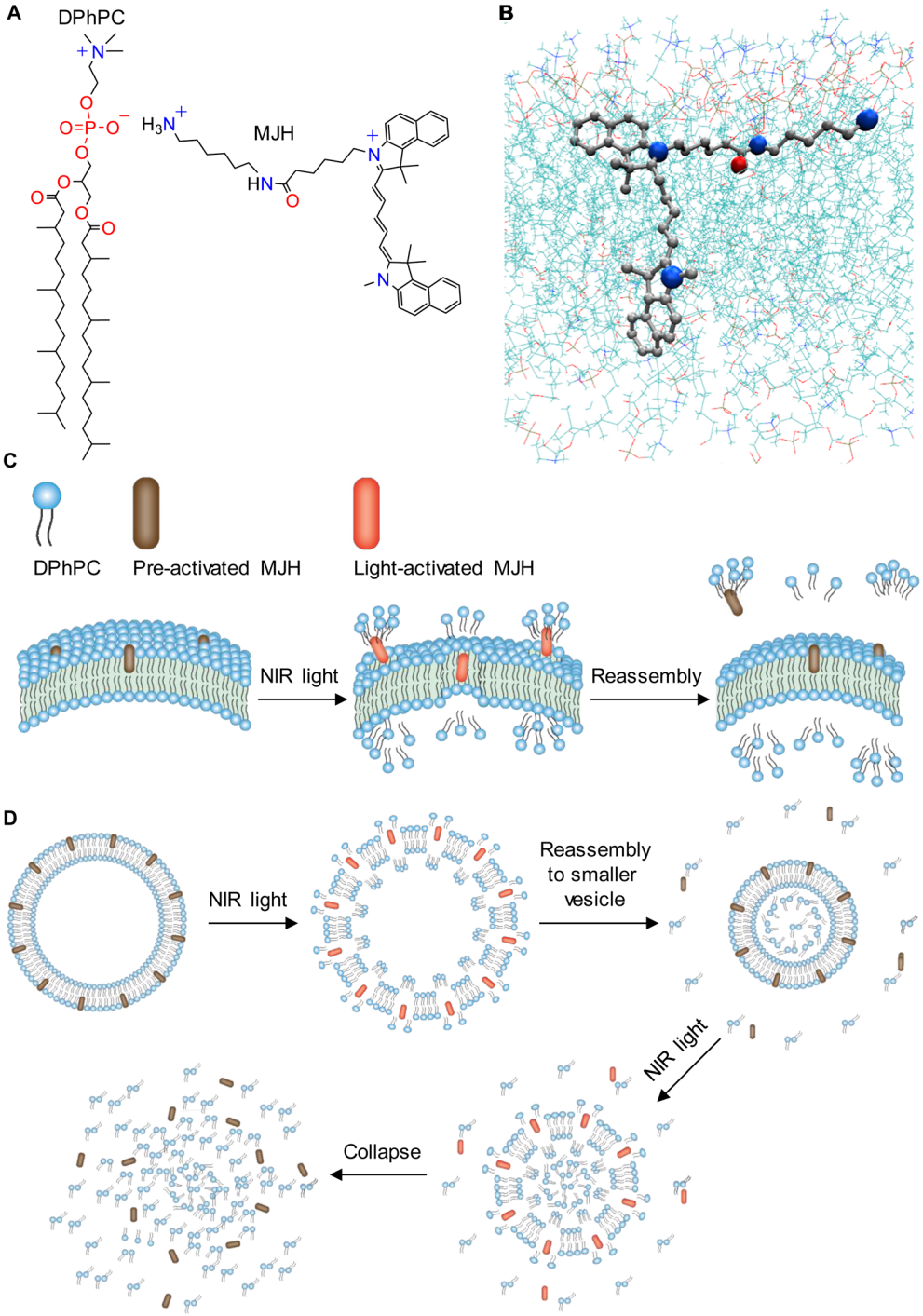

Fig. 2 Molecular-to-microscale model of the plasmon-driven MJH mechanically opening and disassembling of phospholipid vesicles. (A) Chemical structures of DPhPC and the MJH. DPhPC has fully saturated alkyl chains to prevent ROS reactivity in the phospholipid tail. The MJH is Cy5.5-amine. (B) Molecular model of MJH interaction in a phospholipid bilayer, as predicted by MD simulations. The MJH shown in grey, with nitrogen atoms in blue and the oxygen atom in red, is depicted in the center of the phospholipid bilayer section with alkyl chains in cyan and polar heads showing nitrogen atoms in blue, oxygen atoms in red and phosphorus atom in brown. (C) Nanoscale-section model of the mechanical opening, or disassembly, and shrinking of phospholipid bilayers by the plasmon-driven-MJH. (D) Microscale model of the mechanical opening and shrinking of phospholipid vesicles by the plasmon-driven-MJH.

have not detected any expansion of the lipid bilayers, which is typically seen in cavitation and bubble generation processes. This lack of vesicle expansion is a crucial piece of evidence we emphasize to demonstrate that the MJH concept differs from effects such as photothermal and photodynamic processes, where vesicle expansion is also observed. We discuss this aspect herein, and our focus was to show how the action of MJHs is different from those of photothermal or photodynamic processes.

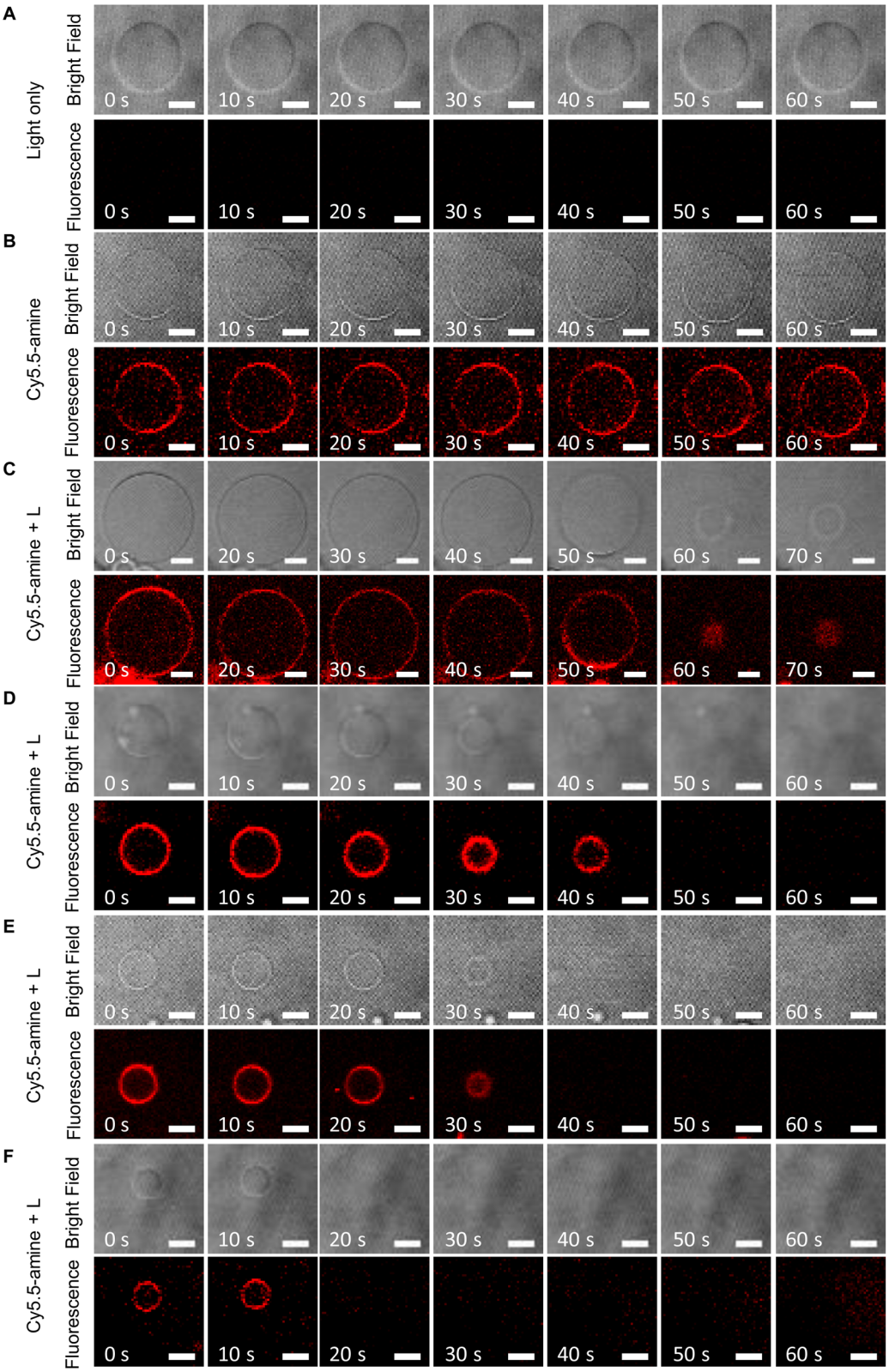

Fig. 3 Time-course treatment of DPhPC GUVs with the MJH Cy5.5-amine with and without light activation. The light activation consisted of laser scanning stimulation at 640 nm with a confocal microscope laser at 5% power (50 μW power; a Plan Apo IR 60×/1.27 water immersion objective). The Cy5.5-amine localization was recorded by imaging at $\lambda_{ex} = 640$ nm, $\lambda_{em} = 663–738$ nm, and 5% (50 μW) laser power every 10 s. (A) DPhPC GUVs treated with 0.1% DMSO (no Cy5.5-amine) as control under light treatment. (B) DPhPC GUVs treated with 2 μM Cy5.5-amine without light activation. (C) DPhPC GUVs of $r_0 = 10.2$ μm treated with 2 μM Cy5.5-amine under VDA photoactivation. (D) DPhPC GUVs of $r_0 = 4.8$ μm treated with 2 μM Cy5.5-amine under VDA photoactivation. (E) DPhPC GUVs of $r_0 = 3.6$ μm treated with 2 μM Cy5.5-amine under VDA photoactivation. Images in panel (E) are adopted from our previous work[23] and analyzed here in a different context. (F) DPhPC GUVs of $r_0 = 2.6$ μm treated with 2 μM Cy5.5-amine under VDA photoactivation.

Additionally, the photoporation results discussed in the literature[44] pertains to pores in the nanoscale to microscale range, since most of these pores are generated using nanoparticle systems. In contrast, the MJH concept operates at the molecular scale, because MJHs are small organic structures that intercalate within the lipid bilayers at a molecular level, as shown in the molecular dynamics simulations presented here. Furthermore, our fluorescence microscopy results indicate the binding of MJHs to the lipid layers.

The force exerted by the MJH Cy5.5-amine is enough to rupture membranes

The force exerted by an MJH was calculated before for Cy7.5 cyanine.[31] The same analysis is applied here to calculate the force exerted by Cy5.5-amine and then to justify that there is sufficient energy in a 640 nm photon to break the membrane if that energy is absorbed and converted by Cy5.5-amine to mechanical energy even with only ~10% efficiency. Interestingly, this 10% efficiency in energy conversion approximately coincides with the energy of the whole-molecule vibration from Raman spectroscopy analysis as described below. This means that the energy contained in the whole-molecule vibration is nearly 10% of the total energy carried by a 640 nm photon for Cy5.5-amine excitation. The 640 nm photon for Cy5.5-amine activation carries $E = hc/\lambda = 3.1 \times 10^{-19}$ J energy (this is equivalent to 1937.2 meV), where h is Planck's constant and c is the speed of light. If the total energy of a 640 nm photon is used for force generation, the generated force would be $F = E/s = 0.31$ nN (considering the size s of the MJH molecule is ~1 nm). Then, for this case, the total stress applied on the membrane is 310 m Nm^{-1}. The mechanical stress required to rupture most membranes[45–49] is only 1–30 m Nm^{-1}. Hence, even if conservatively only 10% of the energy carried by a 640 nm photon is converted to vibrational energy, it would be sufficient to rupture the membrane since $F = 0.031$ nN and stress = 31 m Nm^{-1}. Indeed, by using Raman spectroscopy, the concerted whole-molecule vibrational energy of MJH Cy5.5-amine is $E = 164.9$ meV $= 2.6 \times 10^{-20}$ J (Fig. S4 and Table S1†). Then, for the whole-molecule vibration of MJH Cy5.5-amine, the calculated exerted force is $F = E/s = 0.026$ nN. Thus, the stress applied to the membrane is 26 m Nm^{-1}, which is still in sufficient range to rupture the membrane. Hence, these are ultrafast concerted whole-molecule motions of 40 THz (25 fs for a single oscillation) that can rupture the membrane (ESI Table S1†). A discussion of the molecular displacement and its implications for force calculation and membrane rupture is provided in the ESI on page S23.†

Visualization of plasmon-driven MJH disassembly and shrinking of DPhPC vesicles

Cy5.5-amine emits red fluorescence ($\lambda_{em} = 699$ nm), as shown in Fig. S5 of the ESI.† Using the fluorescence emission properties, the Cy5.5-amine bound to the DPhPC lipid vesicles was localized by fluorescence confocal microscopy at $\lambda_{ex} = 640$ nm and $\lambda_{em} = 663$–738 nm, as shown by the red emission in Fig. 3. Bright field images that do not depend on the fluorescence are shown in conjunction with other images. Bright field observations are independent of dye bleaching. The images indicate that dye bleaching is not taking place. The binding of Cy5.5-amine to DPhPC is a spontaneous and efficient process that occurs immediately upon its addition to the DPhPC vesicle solution and its visualization by confocal microscopy. For the visualization, pictures were recorded every 10 s using $\lambda_{ex} = 640$, dwell time = 2.2 μs per pixel, 50 μW power, and a Plan Apo IR 60×/1.27 water immersion objective. The DPhPC vesicles were observed to start a size reduction, leading to collapse when the plasmon-driven MJH was photoactivated by laser scanning stimulation ($\lambda_{ex} = 640$ nm, dwell time = 2.2 μs per pixel, 50 μW power, and a Plan Apo IR 60×/1.27 water immersion objective), as shown in Fig. 3C–F. The dose energy introduced by continuous laser scanning stimulation of the sample in the presence of Cy5.5-amine was enough for the opening and disassembly of DPhPC vesicles (Fig. 3C–F), while discontinuous scanning every 10 s, with one single laser scan of the sample at a dwell time of 2.2 μs per pixel, was not enough to disassemble DPhPC lipids (Fig. 3B). Continuous laser scanning stimulation over the sample without addition of the MJH does not cause the disassembly of the DPhPC vesicles (Fig. 3A). Additional photos of DPhPC vesicles under these three types of treatments (light only, Cy5.5-amine only, and Cy5.5-amine with light) are presented in the ESI Fig. S6–8.† Fig. 4 shows that the DPhPC vesicle disassembly, shrinkage and collapse is a time-dependent process. The radii of the DPhPC vesicles relative to the initial radius (r/r_0) over time are presented under different conditions. This process is in contrast to the ROS-mediated disruption of lipid bilayers described extensively elsewhere.[35,36] In those studies, the expansion, not contraction, of the lipid bilayers was caused by the reaction and insertion of singlet oxygen into the carbon–carbon double bond in the unsaturated alkyl chain of the phospholipids.[39] This introduced a change of polarity in the alkyl chain that caused the disruption of the lipid bilayers. In those studies, oxidation-resistant DPhPC vesicles were used as controls to prove that ROS from photosensitizers cannot disrupt DPhPC lipid vesicles.[37,38] Interestingly, here, we show that the plasmon-driven MJH disassemble, contract, and collapse DPhPC vesicles that are known to possess good thermal and mechanical stability. In summary, Fig. 3 and 4 support our conclusion that ultrafast vibrational motions by the light-activated plasmon-driven MJH can be transmitted to the adjacent molecules to cause disassembly, contraction, and collapse of the DPhPC vesicles, as proposed by the mechanism depicted in Fig. 2. Our previous study showed that this mechanism is not photothermally induced since light-activated Cy5-amine, a molecule with higher molar extinction than Cy5.5-amine,

The size of the GUV is measured by the initial radius (r_0). The pictures were recorded every 10 s for all the panels. Scale bar: 5 μm. The tiny red dots in the fluorescence channel might be free Cy5.5-amine and/or background fluorescence. It is expected that the free Cy5.5-amine in the aqueous phase might have a lower fluorescence yield than the Cy5.5-amine inserted within the lipid membrane in a non-polar environment, a common behavior observed for free fluorophores *versus* those bound to biological structures.[50]

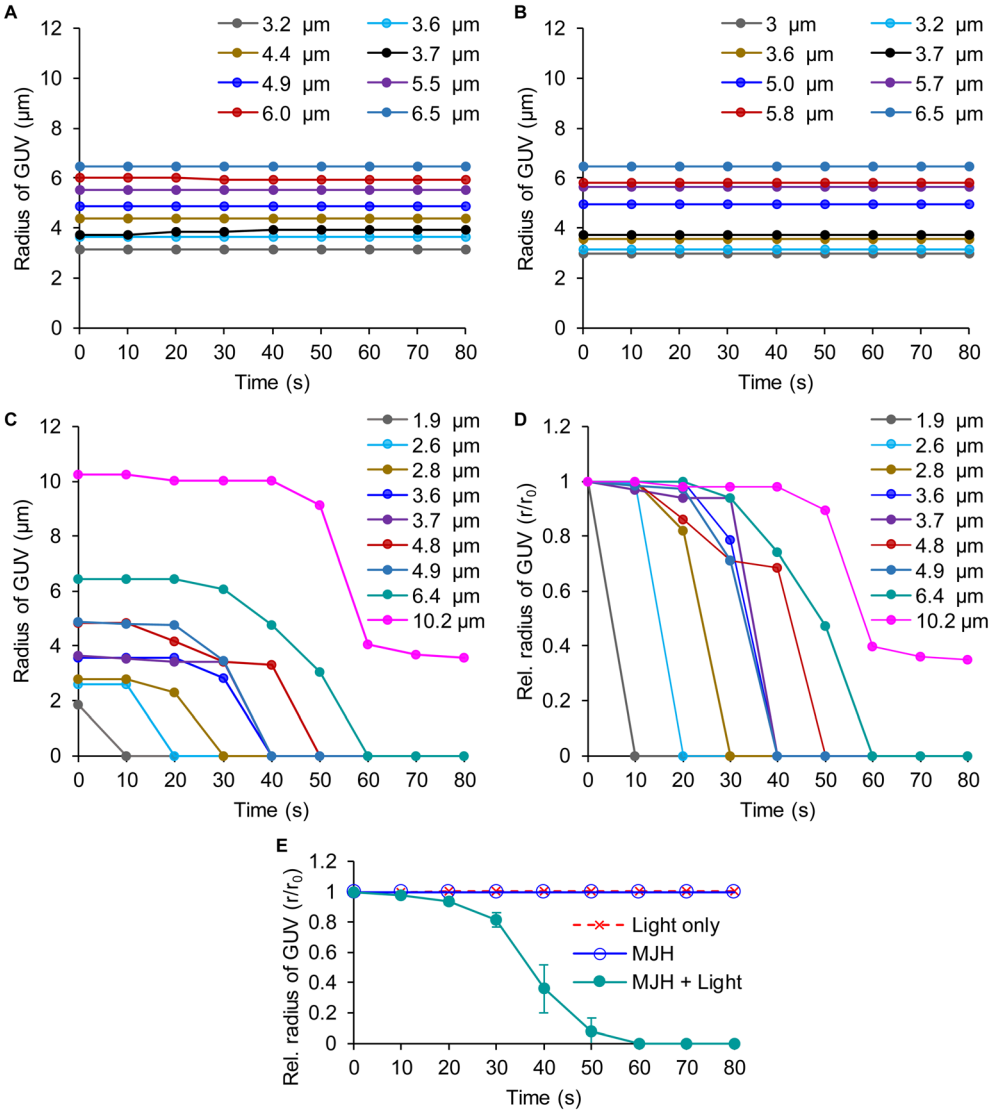

Fig. 4 Time-course disassembly of DPhPC GUVs of various sizes with MJH Cy5.5-amine and with light activation. The size of the GUV is measured by its radius (r) over time, with its initial radius = r_0 from images, as shown in Fig. 3 and ESI Fig. S6–8.† The MJH Cy5.5-amine is used at a concentration of 2 μM. (A) The radii of various ($n = 8$) DPhPC GUVs under light treatment only. (B) The radii of various ($n = 8$) DPhPC GUVs under treatment with Cy5.5-amine only. (C) The radii of various ($n = 9$) DPhPC GUVs under treatment with Cy5.5-amine and with light activation. (D) The relative radius (r/r_0) of the GUV over time when treated with Cy5.5-amine and with light activation. The data labels correspond to the initial radius (r_0) of the GUV. (E) Averaged relative radius (r/r_0) of the GUV over time and comparison between experimental groups. The relative radius was averaged for GUVs with sizes between 3.6 and 6.5 μm. The data are presented as the mean ± SD ($n = 5$). The SD values for the light-only control and MJHs are smaller than the size of the data points.

did not break the DPhPC vesicles under comparable conditions as in Fig. 3, which suggested that Cy5-amine is a weaker MJH.[23] This observation was supported by the measurement of a weaker plasmonicity index for Cy5-amine *versus* Cy5.5-amine.[31]

Size-dependent mechanical disassembly and shrinking of DPhPC vesicles

Initially, the purpose of replicating the experiment of DPhPC vesicles under various conditions was to calculate and compare averaged measurements (*e.g.*, the time of collapse) among the experimental group (Cy5.5-amine with light activation) and the

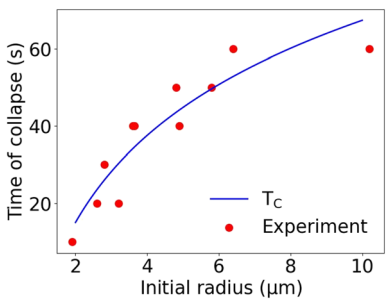

Fig. 5 Validation of the theoretical model. T_c is given by eqn (1). Fitting leads to the phospholipid removal constant rate $k = 0.0614\ s^{-1}$; $r_c = 1.26$ μm.

controls. However, we discovered that the disassembly and shrinking of DPhPC vesicles is a size-dependent process that is reflected in the time required for the final collapse (Fig. 4). The larger the DPhPC vesicle, the more the DPhPC molecules are present in the vesicle. Therefore, it took longer to eject the molecules, as observed in Fig. 4. The vesicle of initial radius $r_0 =$ 2.6 μm collapsed in 10–20 s, $r_0 = 3.6$ μm collapsed in 30–40 s, r_0 = 4.8 μm collapsed in 40–50 s, and $r_0 = 10.2$ μm did not completely collapse even at 70 s (Fig. 3C). In Fig. 3C, it can be observed that Cy5.5-amine is also depleted from the lipid bilayer over time, allowing the vesicle to reach a stable intermediate state as observed at 70 s. For larger GUVs, it takes more time to eject the lipids; hence, the MJH will be exposed longer to the light. As such, some fraction of Cy5.5-amine will photobleach over a prolonged period of exposure, reducing the number of active MJHs. The size-dependent shrinking of the lipid vesicle supports the mechanism proposed in Fig. 2, including that some Cy5.5-amine is ejected from the lipid bilayer, allowing the vesicle to reach a stable intermediate reduced size. In contrast, ROS-mediated events typically lead to deformed and/or expanded lipid bilayers.[39]

Theoretical model that fits the size-dependent mechanical disassembly of lipid vesicles

Our model assumes that plasmon-driven MJHs remove phospholipids at a constant rate, k. Thus,

$$N = N_0 e^{-kt}$$

where N_0 is the initial number of phospholipids in the membrane. Substitution of $N \sim r^2$, where r is the radius of the membrane, leads to eqn (1):

$$T_c = \frac{2}{k}(\ln(r_0) - \ln(r_c)) \quad (1)$$

where r_c is the critical radius of the membrane, below which the self-assembly of phospholipids is not possible. r_0 is the initial radius of the membrane and k is the removal constant rate. This theoretical model fits reasonably well with the experimental observations, the size-dependent time of collapse (T_c), as shown in Fig. 5.

Disassembly of multilayered non-concentric *versus* concentric DPhPC lipid vesicles

Disassembly of multilayered DPhPC lipid vesicles provides further evidence that a mechanical action is responsible since multilayers introduce another level of mechanical stability and different mechanical properties (Fig. 6). For example, the non-concentric DPhPC vesicles in Fig. 6A show faster shrinkage and collapse of the internal bilayer than the outer bilayer due to the outer bilayer's larger size, as shown in Fig. 6C. In contrast, for two concentric DPhPC vesicles of similar sizes (Fig. 6B), both lipid bilayers are in proximity and their molecular surfaces might be interacting, which should increase the overall mechanical stability of the vesicles. The lipids from the internal bilayer might not be easily ejected because the outer lipid bilayer prevents it, and the lipids from the outer lipid bilayer cannot be easily ejected inwards because it is prevented by the internal bilayer. The two layers appear to merge, stabilizing each other. Therefore, this structure is mechanically more stable and takes longer to disassemble by light-activated MJH, as suggested by the observations in Fig. 6B and D.

Plasmon-driven MJHs open cellular membranes and cause shrinking of the cell

Interestingly, human melanoma A375 cells treated with light-activated MJHs resulted in opening of the cellular membranes and then shrinking of the cells, as shown in Fig. 7A–D. Here, we excite the plasmon mode in cell-membrane-bound Cy5.5-amine using 640 nm-laser scanning stimulation in confocal microscopy, which results in the permeabilization of the cellular membrane to 4′,6-diamidino-2-phenylindole (DAPI). The intracellular DAPI predominantly stains by DNA intercalation when access is enabled by membrane disruption, as illustrated in Fig. 7B. In viable cells, DAPI is a very slow cell membrane permeable dye, as observed in the controls (Fig. 7A–D). This is consistent with previously observed results.[31] However, in contrast, here, the Cy5.5-amine was added to the cells and immediately photoactivated, while the Cy5.5-amine was mainly bound to the external cell membrane (Fig. S9 of the ESI†). Fig. S9A–D† show the Cy5.5-amine localization in the same cells, as shown in Fig. 7A–D, respectively. This process resembles the mechanical disassembly and shrinking of GUVs observed in Fig. 3 and 4 since the Cy5.5-amine were bound to the external cell membranes by the time of light activation (Fig. S9†). Permeabilization of A375 cells in Fig. 7A–D was replicated ($n = 4$), and the statistical analysis is shown for 42 cells in each group in ESI Fig. S10.† These results support our conclusion that the permeabilization to DAPI was caused by the mechanical opening of the external cellular membrane.

The permeabilization of A375 cell experiment was replicated at different concentrations of 2 μM and 4 μM, as shown in Fig. S11 and 12 of the ESI.† As expected, at higher concentrations of Cy5.5-amine, more pores are formed and more DAPI enters the cells, as shown by the more intense blue nuclear fluorescence. In an experiment using 4 μM Cy5.5-amine, the cell membrane was destroyed, and ~7 min later the cell membrane fragments reassembled to form satellite lipid vesicles around the destroyed cell, as shown in Fig. S13B (arrows) of ESI.† This is indirect evidence for the mechanical disassembly of cellular membranes since the phospholipid vesicle reassembly occurs.

The mechanical action of plasmon-driven MJHs is distinct from photothermal and photodynamic effects

To provide further evidence that the cell membranes were opened mechanically by light-activated MJHs and not by a thermal effect, we measured the temperature of the media while a cell suspension of 2×10^5 cells mL^{-1} was treated (Fig. 7E and S14A†). There was little thermal (1 °C after 10 min of irradiation using a 630 nm LED light at 80 mW cm^{-2}) heating of the cell suspensions when treated with the plasmon-driven MJH. The temperature curve in the light-activated Cy5.5-

amine solutions of 2 μM or 4 μM concentration overlaps with the temperature curve of the light treatment control (0.1% DMSO + 630 nm LED light at 80 mW cm^{-2} for 10 min). The concentrations of Cy5.5-amine of 2 μM or 4 μM are considered too low to provide a low optical absorption density and insufficient to cause photothermal heating. Fig. S14A of the ESI† shows an enlargement of the temperature axis to emphasize the details of the temperature curves. For comparison, cells were treated thermally by heating the cell suspension at 54 °C for 10 min (see Fig. S14† for details on thermal treatments). The membrane permeabilization to DAPI was quantified by flow cytometry (Fig. 7F). The results show that the plasmon-driven MJH can permeabilize the cells to DAPI, while thermal treatment at 54 °C for 10 min did not permeabilize the cells. Longer thermal treatment for 30 min at 54 °C did lead to permeabilization the cells, likely due to protein denaturalization, disruption of cellular functions, and ultimately to cell death.[51–55] These findings support the conclusion that the light-activated MJH permeabilize cells within 10 min or less by a process that does not induce heating and is different from a thermal treatment. Our findings on MJHs agree with others who have independently demonstrated whole-molecule vibration, in other molecular systems, demonstrating a mechanical action and not simply a thermal heating process.[28,29]

Vibrational energy transfer (VET) is fundamentally a mechanical process, not simply a thermal process.[25,28] In

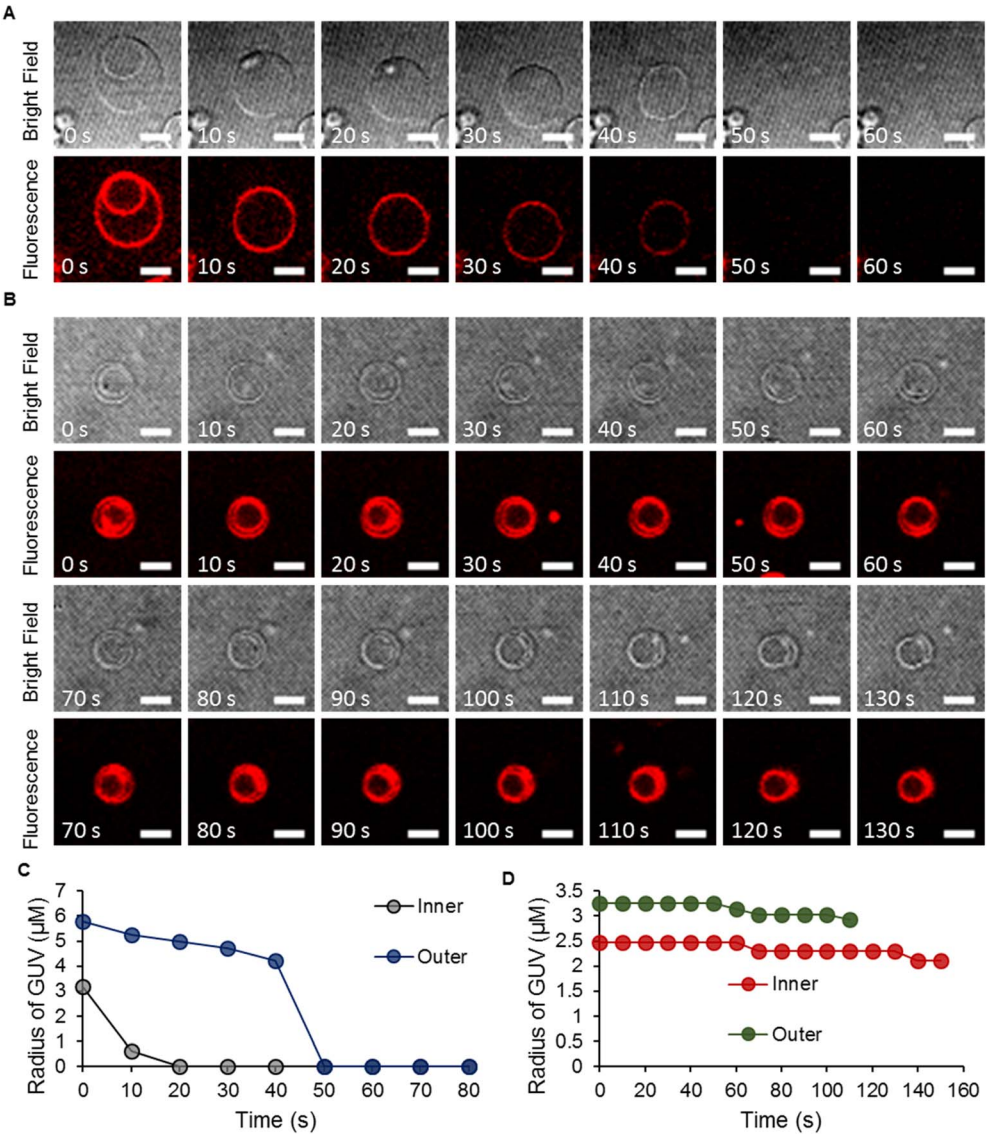

Fig. 6 Time-course disassembly of multilayered non-concentric *versus* concentric DPhPC GUVs with light-activated MJH. The GUV radius (r) over time with an initial radius of r_0. The Cy5.5-amine is at a concentration of 2 μM. Light activation consisted of continuous exposure to a 640 nm confocal microscope laser light at 5% power (50 μW; a Plan Apo IR 60×/1.27 water immersion objective). Cy5.5-amine is observed in the fluorescence channel by imaging at $\lambda_{ex} = 640$ nm, $\lambda_{em} = 663–738$ nm, and 5% (50 μW) laser power every 10 s. (A) One non-concentric GUV encapsulated in a larger GUV. (B) One concentric GUV encapsulated in a larger GUV. (C) The radius of the two non-concentric GUVs over time from panel (A). (D) The radius of the two concentric GUVs over time from panel (B). The pictures were recorded every 10 s for all the panels, $n = 1$. Scale bar: 5 μm.

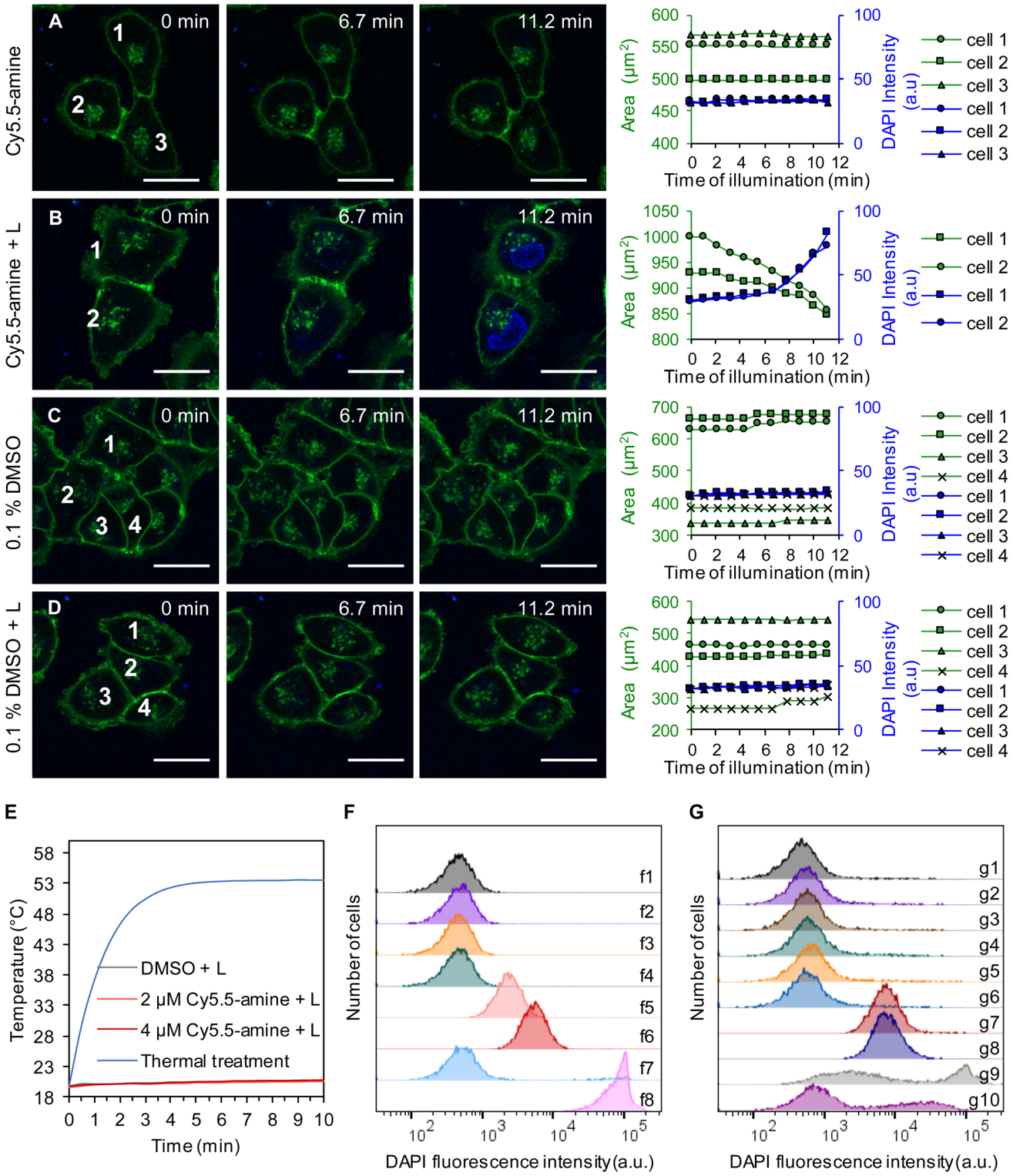

Fig. 7 Cell membrane permeabilization by plasmon-driven MJHs in A375 cells is distinct from photothermal or photodynamic therapy. Permeabilization of DAPI into the cells and the size of the cells were recorded as a function of time (rightmost column). (A) Cells in the presence of 2 μM Cy5.5-amine without laser irradiation. (B) Cells in the presence of 2 μM Cy5.5-amine with 640 nm laser irradiation. (C) Cells in the presence of 0.1% DMSO control without laser irradiation. (D) Cells in the presence of 0.1% DMSO with 640 nm laser irradiation. The irradiation times are shown in each image. For the activation of the MJH effect, the cells were irradiated at $\lambda_{ex} = 640$ nm and 25% power (210 μW). The pictures were recorded every 1 min. CellMask Green is a cell membrane stain; $C_{loading} = 5$ μg mL^{-1} for 30 min, $\lambda_{ex} = 488$ nm, and $\lambda_{em} = 500–550$ nm. Loading concentration of DAPI: $C_{loading} = 1$ μM, $\lambda_{ex} = 405$ nm, and $\lambda_{em} = 425–475$ nm. Representative confocal images of each condition are shown. The experiment in panels A–D was replicated ($n = 4$), and statistical analysis is shown for 42 cells in each group in ESI Fig. S10.† All scale bars = 25 μm. (E) Temperature of the media ($n = 3$) while cells were treated with 630 nm LED light and MJH (Cy5.5-amine). A more detailed 18.5 to 21.5 °C temperature axis is shown in ESI Fig. S14† to illustrate the details of the overlap between DMSO + L, 2 μM Cy5.5-amine + L and 4 μM Cy5.5-amine

energy transport in nanostructures or molecular junctions, vibrational modes may transfer energy coherently without or minimized heat dissipation. In systems where vibrational coherence or resonance dominates, energy transfer may avoid dissipation and stay directed. The literature refers to this last case, a coherent optomechanical conversion, a type of non-dissipative energy transfer.[28,29] This is to show it is possible to observe this type of phenomenon. The authors measured the mechanical (vibrational) contribution of a molecule in an optomechanical process where plasmons are involved. This gives support to the mechanical effects inferred in molecular jackhammers since they are related processes.[44]

Previously, we studied the thermal effects in light-activated indocyanine green (ICG). The photothermal effects are directly proportional to the absorption cross-section, also known as molar extinction, and to the concentration of the molecules or light-absorbing nanoparticles.[30] The cyanine dye ICG is a commonly known photothermal and photodynamic agents to cause slow apoptotic cell death through oxidative stress.[56] In contrast, MJH action results in a rapid cell membrane permeabilization within minutes at concentrations of 4 μM or below where the thermal effects are negligible. We have shown that only at 8 μM concentration in ICG, the photothermal effects start playing a role, and it causes only a 1 °C temperature increase.[23] However, ICG led to negligible cell membrane permeabilization in 0.8% of the cell population, as observed with a 730 nm light dose of 80 mW cm^{-2} for 10 min.[23] ICG at 32 μM concentration caused a ~3 °C increase, which resulted in a minor 2% permeabilization of cells. At 100 μM ICG, only 13% of the cells were permeabilized with a ~6 °C increase. We have shown that ICG is not an efficient agent for rapid permeabilization of cancer cells under comparable conditions used for the MJH. The efficient photothermal killing of cancer cells using ICG requires high light intensities (1 to 4 W cm^{-2}) and high concentrations of ICG (~50 to 100 μM).[57,58]

To provide evidence that photodynamic therapy ROS-mediated chemical effects are not responsible for the MJH opening of the cellular membranes, we conducted experiments in the presence of ROS scavengers, 100 mM thiourea and 2.5 mM sodium azide, as shown in Fig. 7G. The results show that ROS scavengers do not delay the action by the plasmon-driven MJH to permeabilize cells to DAPI (Fig. 7G, raw g7 is without ROS scavengers while raw g8 is with ROS scavengers). These results are consistent with previous ROS inhibition experiments in Cy7.5 cyanines.[31] We confirmed that the ROS scavenger mixture, 100 mM thiourea and 2.5 mM sodium azide, is effective in delaying the ROS-mediated permeabilization in cells when treated for 1 h with 50 mM H_2O_2, a highly reactive hydroxyl radical source (Fig. 7G, raw g10). However, a short treatment time of 10 min with 50 mM H_2O_2 is not enough to permeabilize the cells (Fig. S15 and 16 in the ESI†). In addition, 1 mM or 6 mM H_2O_2 for 1 h is ineffective in permeabilizing cells (Fig. S16B and C†). These findings support the conclusion that ROS-mediated permeabilization is a slow process that takes longer than 10 min, requires relatively high concentrations of ROS, and that induces oxidative stress by chemical modifications of the cellular structures, leading to slow cell death-mediated opening of cell membranes.[59,60] Overall, these findings support our conclusion that plasmon-driven MJHs permeabilize the cells by molecular mechanical action through a process that is not delayed by ROS scavengers and does not induce heating of the media.

Flow cytometry analysis confirms that plasmon-driven MJH-mediated mechanical action is distinct from thermal effects

We compared the characteristics of the A375 cells treated with plasmon-driven MJHs *versus* those that were thermally treated using flow cytometry analysis (Fig. 8). The results show that plasmon-driven MJH-permeabilized cells (Fig. 8D) have a different morphological complexity than the thermally treated cells (Fig. 8F), as revealed by the different light scattering properties in flow cytometry. The thermal mechanism follows a two-step process (red arrows) that is different when compared to the mechanical mechanism (Fig. 8F). The first step in thermal mechanism could be due to the generalized denaturalization of biological structures and the second step to the membrane opening. Both populations, mechanically treated and thermally treated, are combined in a single plot (Fig. 8H and I) that shows that these are distinct cell populations. This confirms that mechanical opening of cells is a process separate from thermal treatment. While the plasmon-driven MJH mechanically opens the cell membranes through a fast process (<10 min), the thermal treatments at 54 °C denatures cellular structures, such as proteins, DNA and lipid membranes, leading to a generalized change in the cellular structure and morphology through a temperature-dependent slower process.[51,55]

+ L. This treatment is done for the cell suspension for the purpose of measuring the cell permeabilization by flow cytometry while measuring the temperature of the solution. (F) Flow cytometry analysis of the plasmon-driven MJH permeabilization of cells. Cells treated with 0.1% DMSO only (f1), cells treated with 0.1% DMSO + light (f2), cells treated with 2 μM Cy5.5-amine (f3), cells treated with 2 μM Cy5.5-amine (f4), cells treated with 2 μM Cy5.5-amine + light (f5), cells treated with 4 μM Cy5.5-amine + light (f6), cells thermally treated to 53.6 °C for 10 min (f7), and cells thermally treated to 53.6 °C for 30 min (f8). Light treatments consisted of a 630 nm LED at 80 mW cm^{-2} for 10 min. (G) Flow cytometry analysis shows that ROS scavengers do not inhibit the permeabilization of cells by plasmon-driven MJHs. Cells treated with 0.1% DMSO only (g1), cells treated with 0.1% DMSO + 100 mM thiourea + 2.5 mM sodium azide (g2), cells treated with 0.1% DMSO + light (g3), cells treated with 0.1% DMSO + 100 mM thiourea + 2.5 mM sodium azide + light (g4), cells treated with 4 μM Cy5.5-amine (g5), cells treated with 4 μM Cy5.5-amine + 100 mM thiourea + 2.5 mM sodium azide (g6), cells treated with 4 μM Cy5.5-amine + light (g7), cells treated with 4 μM Cy5.5-amine + 100 mM thiourea + 2.5 mM sodium azide + light (g8), cells treated with 50 mM H_2O_2 for 1 h (g9), and cells treated with 100 mM thiourea + 2.5 mM sodium azide + 50 mM H_2O_2 for 1 h (g10). Light treatments consisted of a 630 nm LED at 80 mW cm^{-2} for 10 min. The experiment with ROS scavengers was replicated (n = 4), and results are shown in ESI Fig. S15.† All the cell suspensions for this study contained 0.1% DMSO, which is used to pre-solubilize the cyanine MJH in 2 mM or 4 mM stock solution.

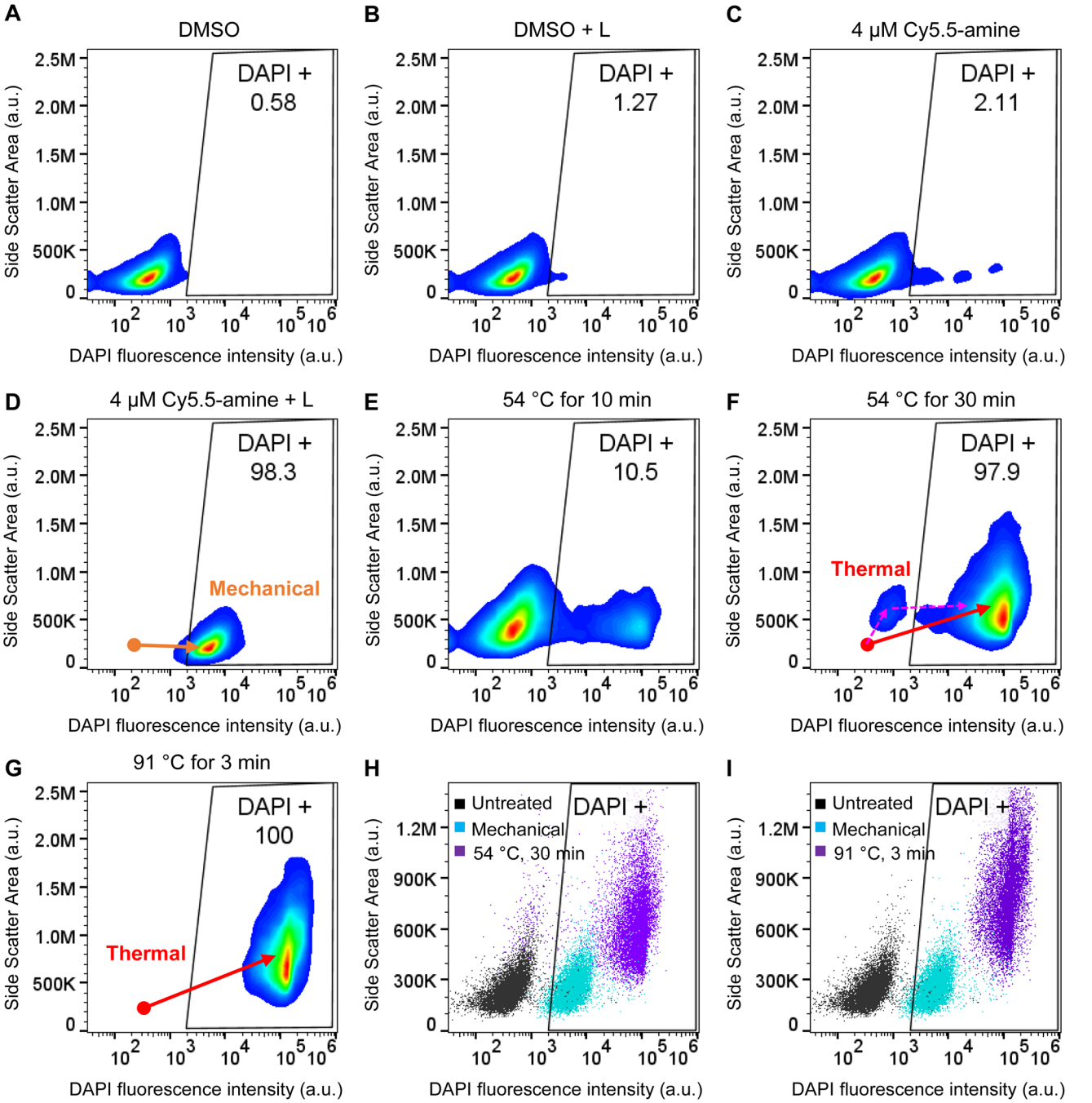

Fig. 8 Mechanical and thermal cell permeabilization are distinct processes, as revealed by flow cytometry analysis. (A) Cells treated with 0.1% DMSO as the control. (B) Cells treated with 0.1% DMSO and light. (C) Cells treated with 4 μM Cy5.5-amine. (D) Mechanical treatment: cells treated with 4 μM Cy5.5-amine + light. (E) Thermal treatment at 54 °C for 10 min. (F) Thermal treatment at 54 °C for 30 min. The dashed arrows show the progression to the final position shown by the solid arrow. (G) Thermal treatment at 91 °C for 3 min. (H) Comparison of mechanical treatment *versus* thermal treatment at 54 °C for 30 min. (I) Comparison of mechanical treatment *versus* 91 °C for 3 min. Light treatments consisted of a 630 nm LED at 80 mW cm^{-2} for 10 min. Cell suspensions for this study contained 0.1% DMSO, which is used to pre-solubilize the cyanine molecule in 2 mM or 4 mM stock solution in DMSO.

Conclusions

Cyanine Cy5.5-amine is a molecular plasmon which upon photon activation of its vibronic mode can induce a concerted whole-molecule stretching with a vibrational frequency of 40 THz. This is seven orders of magnitude faster than the Feringa-based motors that we used in previous studies.[23] This process allows the conversion of photon energy to mechanical energy, which can be used for remote-controlled spatiotemporal mechanical work at the molecular level. Here, we demonstrated that we can mechanically open synthetic lipid vesicles and cellular membranes using plasmon-driven MJHs. We proposed

a mechanism for the stepwise mechanical process for shrinking the membranes by plasmon-driven MJHs. This molecular mechanical mode of action is distinct from the thermal and ROS-mediated chemical processes. The molecular mechanical action opens vacancies in synthetic vesicles within seconds, and permeabilization of cells causes necrotic cell death in <10 min. The mechanical action does not cause thermal killing, nor is it inhibited by ROS scavengers. In contrast, thermal treatments at ~55–65 °C for a short time (10–15 min) in mammalian cells is well known to cause slow programmed cell death by apoptosis.[55] Similarly, ROS is well known to cause oxidative stress in cells, leading to slower apoptotic cell death.[59] High concentrations (50 mM H_2O_2) with long exposure times (~1 h or longer) are required to permeabilize cells.[59] In agreement with this, previously, we have shown that high levels of singlet oxygen generated by a photosensitizer did not permeabilize cell membranes at short reaction times (within 10 min).[23] In summary, here, we have provided strong evidence that light activated cyanines act as plasmon-driven MJHs that open lipid membranes by mechanical action within seconds even when the phospholipids are composed of fully saturated alkyl chains.

Materials and methods

Cyanine molecule

Cy5.5-amine was purchased from Lumiprobe Corp. (Maryland, USA).

LED illumination system

A 630 nm LED (model UHP-F-630) illumination system was purchased from Prizmatix, Israel.

Synthesis of DPhPC giant unilamellar vesicles (GUVs)

GUVs were synthesized using the gel-assisted formation method with minor modifications.[61,62] Briefly, the fully saturated DPhPC phospholipid (1,2-diphytanoyl-*sn*-glycero-3-phosphocholine, Avanti Polar Lipids, product #850356) was dissolved in anhydrous chloroform at 1 mg mL^{-1} concentration and stored at −20 °C. A microscope cover glass was flame-cleaned for ~5 s in a Bunsen burner. Then, 250 μL of 5% (w/v) polyvinyl alcohol (PVA, 145 kDa, MilliporeSigma) in deionized water was applied dropwise and spread on the surface of the cover glass and dried overnight at 50 °C. Then, 30 μL of 1 mg mL^{-1} DPhPC solution in chloroform was applied dropwise on the surface of the PVA-coated cover glass and dried at room temperature overnight. Subsequently, ~250 μL of PBS buffer (Corning product # 21040CV) was added to allow the hydration and formation of GUVs for ~1–2 h. Then, the GUVs were harvested by pipetting up-and-down to help detach the GUVs from the surface. GUVs were then transferred to an Eppendorf tube and stored at 4 °C until use. The GUVs were utilized as soon as possible, ideally on the same day of preparation and no longer than 2 d after the initial preparation.

Photoactivation of plasmon-driven MJHs and the GUV disassembly experiment

GUV suspension in PBS buffer (5 μL) was applied dropwise onto the surface of a glass microscope slide and then mixed with 5 μL of 2 μM Cy5.5-amine solution in PBS buffer containing 0.1% DMSO. DMSO was used to pre-solubilize and store the Cy5.5-amine as 2 mM stock solution at −20 °C. On the day of the experiment, fresh 2 μM Cy5.5-amine was prepared in PBS buffer using 1 : 1000 dilution from the 2 mM stock solution in DMSO. Immediately after mixing GUVs and Cy5.5-amine, the mixture was covered with a microscope cover slide, and the GUVs were visualized using a confocal microscope model Nikon A1-Rsi (Rice University Shared Equipment Authority). The GUVs were recorded in a time-series photoactivation protocol using a Galvano laser scanner and A1 stimulation and ND stimulation dialog boxes. Photoactivation consisted of exposure to 640 nm laser scanning at 5% power (50 μW power), dwell time = 2.18 μs, and using a Plan Apo IR 60×/1.27 water immersion objective. Fluorescence images were recorded at λ_{ex} = 640 nm and λ_{em} = 663–738 nm at 5% (50 μW) laser power every 10 s. For the non-irradiated controls, the images were recorded every 10 s using the same imaging parameters. The NIS-Elements AR5.21.03 software was used for data analysis (Rice University Shared Equipment Authority) such as measuring the size of liposomes over time.

Cell culture of human melanoma A375 cells

The human wild-type A375 cell line, originally isolated from a female patient with melanoma, was obtained from ATCC (CRL-1619, batch number 70032966). Cells were cultured in 10 cm polystyrene tissue culture treating dishes (Corning) containing DMEM with L-glutamine, 4.5 g L^{-1} glucose, and sodium pyruvate (Corning Inc. 10013CV) and supplemented with 10% FBS (Corning, 35010CV), 1× MEM vitamin solution (Gibco, 11120052), 1× MEM non-essential amino acid solution (Gibco, 11140050) and penicillin/streptomycin (Gibco, 15140–122). Typically, 0.5–1 million cells were inoculated per dish, cultured for 3–4 d in an incubator at 37 °C and 5% CO_2, and then transferred to a new dish when confluency reached nearly 90%. For the passage step, cells were detached with 0.05% trypsin–EDTA (Gibco, 25-300-054).

Photoactivation of plasmon-driven MJHs in cancer cells using confocal microscopy

For confocal microscopy, 80,000 A374 cells were inoculated in a glass bottom dish (IBIDI, μ-Dish 35 mm high glass bottom) containing DMEM with all supplements as described before and cultured at 37 °C and 5% CO_2 for 1 day. On the day of the photoactivation experiment, the DMEM was removed, and the cells were washed once with PBS buffer. Then a mixture of fresh DMEM without phenol red was added to the cells. The DMEM without phenol red (GenClone, product number 25-501C) was supplemented with 10% FBS (Corning, 35010CV), 1× MEM non-essential amino acid solution (Gibco, 11140050) and penicillin/streptomycin (Gibco, 15140-122). CellMask Green dye was

added to the media as a stain to visualize the plasma membrane ($C_{loading} = 5$ μg mL^{-1}; $\lambda_{ex} = 488$ nm and $\lambda_{em} = 500$–550 nm) and incubated for 30 min at 37 °C and 5% CO_2. Then, the MJHs (Cy5.5-amine at 2 μM or 4 μM) were added to the media and immediately, without incubation, the cells were subjected to confocal microscopy for photoactivation. DAPI was added to the cells ($C_{loading} = 1$ μM; $\lambda_{ex} = 405$ nm and $\lambda_{em} = 425$–475 nm), and the cells were transported to the microscopy room. Typically, it took ~7 min to take the cells to the microscopy room, focus the cells, set up the imaging parameters, and initiate the photoactivation. The cells were imaged and photoactivated in a time-series photoactivation protocol using a Galvano laser scanner and A1 stimulation and ND stimulation dialog boxes in the confocal microscope model Nikon A1-Rsi (Rice University Shared Equipment Authority). For the photoactivation of Cy5.5-amine, a $\lambda_{ex} = 640$ nm laser was used at 25.0% (250 μW), with dwell time = 2.18 μs, and using a Plan Apo IR 60×/1.27 water immersion objective for periods of 1 min and 10 stimulation periods in total. In between each stimulation period, images of the CellMask Green, DAPI and red fluorescence channel (Cy5.5-amine) were simultaneously recorded. The imaging frame of CellMask Green was recorded using the parameters of$\lambda_{ex} =$ 488 nm, $\lambda_{em} = 500$–550 nm, laser power intensity = 5.0% and detector sensitivity = 25 HV. Simultaneously, DAPI staining was recorded using the parameters of $\lambda_{ex} = 405$ nm, $\lambda_{em} = 425$–475 nm, laser power intensity = 5.0% and detector sensitivity = 100 HV. For the imaging of Cy5.5-amine, the parameters $\lambda_{ex} =$ 640 nm, $\lambda_{em} = 663$–738 nm, detector sensitivity = 100 HV and laser power = 1.0% were used. The area of the cell and DAPI intensity in the nucleus of the cell were measured over time using the NIS-Elements AR5.21.03 software. The area of the cell was delineated by the perimeter of the CellMask Green staining at the cellular membrane.

Plasmon-driven MJH activity and flow cytometry analysis

A375 cells were cultured as described before. Two days before the treatment, cells were inoculated at 2 million cells per dish (10 cm polystyrene tissue culture dishes). The cells were harvested using 0.05% trypsin–EDTA (Gibco, 25-300-054), then the cells were counted and adjusted to a cell density of 2×10^5 cells mL^{-1} in DMEM with L-glutamine, 4.5 g L^{-1} glucose, and sodium pyruvate (Corning Inc. 10013CV) and supplemented with 10% FBS (Corning, 35010CV), 1× MEM vitamin solution (Gibco, 11120052), 1× MEM non-essential amino acid solution (Gibco, 11140050) and penicillin/streptomycin (Gibco, 15140–122). 1 mL of this cell suspension containing 2×10^5 cells was used in each treatment. In a 1.5 mL Eppendorf tube, 1 μL of stock solution containing 2 mM Cy5.5-amine (or other concentrations or 0.1% DMSO control) in DMSO (Fisher, 99.7%) was placed in the bottom of the tube, then 1 mL of the cell suspension was added into the tube to obtain a final concentration of 2 μM Cy5.5-amine containing 0.1% DMSO and 2×10^5 cells. The mixture was then incubated at 37 °C and 5% CO_2 for 30 min. Then, 1 μM DAPI was added into the cell suspension, and it was transferred to a 35 mL polystyrene tissue culture dish. The cells were immediately treated under NIR light at 630 nm and 80 mW cm^{-2} for 10 min using a LED light source (Prizmatix UHP-F-630, Israel) to illuminate the entire dish. When the cells were treated, the dish was placed on top of an aluminum block painted black, so that the excess NIR light was not reflected into the cell suspension. The aluminum block also acted as a heat-sink, maintaining a constant temperature in the dish during the irradiation. The instrument for flow cytometry analysis (SONY, MA900 Multi-Application Cell Sorter) was set up and calibrated and was ready for analysis of the photoactivated samples. Therefore, as soon as the 10 min light treatment completed, the cell suspension was rapidly transferred from the 35 mm dish to a flow cytometry tube, and the cells were analyzed for DAPI permeabilization. It took ~30 s to load the sample and to start cell counting. Permeabilization of cells was measured as DAPI positive cells. The light intensity was measured using an Optical Power Meter from Thorlabs, sensor model S302C and console model PM100D. For the ROS scavenger experiment, the same procedure was followed except that 100 mM thiourea and 2.5 mM sodium azide were added to the cell suspension containing 2×10^5 cells mL^{-1}. Thiourea was prepared as a 2.5 M stock solution in sterile DI water and sodium azide as a 2.5 M stock solution in sterile DI water. This mixture of ROS-scavengers was previously used and validated.[23]

Temperature measurements

Permeabilization of the cells and flow cytometry analysis were conducted as described above. The temperature of the cell suspension was measured using a temperature probe (model SC-TT-K-30-36 PP; Omega Engineering, Inc.) immersed in the media during NIR light illumination. The temperature of the media remained nearly constant at room temperature of ~20 °C upon illumination of the media with a 630 nm LED light at 80 mW cm^{-2} for 10 min. There was only a minor temperature increase of ~1 °C that is attributed to the light illumination absorption by the components of the media.

Molecular dynamics simulations

We performed all-atom molecular dynamics (MD) simulations to compare the positioning of Cy5.5-amine inside POPC:POPE:POPG or DPhPC membranes. The simulations were performed with the open-source code NAMD[63,64] and CHARMM36 force field.[65,66] The initial configuration of the simulation systems was prepared by CHARMM-GUI.[67] The parameters for Cy5.5-amine were generated using the CHARMM-GUI Ligand Modeler.[68] Next, we performed geometric optimization at the HF-3c level of theory using the ORCA package.[69] CHARMM-GUI Membrane Builder was used to build membranes.[70–73] DPhPC membrane has 156 molecules on each layer. POPC:POPE:POPG has 80 POPC, 40 POPE, and 8 POPG molecules. The overall charge of the membrane and Cy5.5-amine molecules was neutralized by adding sodium counterions. Additionally, 3 nm of TIP3P water was added with 150 mM NaCl buffer to simulate the ionic strength used in the experiments. We let the system equilibrate in an NPT ensemble at 303.15 K. Initially, the Cy5.5-amine molecules were placed in the middle of the membrane. During the first 225 ps, constraints limit the movement of both

lipid heads and the Cy5.5 amine. Subsequently, we eliminated all constraints, enabling the system to reach equilibrium by 10,000 ps.

Time-dependent density functional theory (TDDFT) analysis

Starting from the ground-state DFT calculation to obtain the energies of all the occupied levels, the absorption spectra were calculated using TDDFT and the Liouville-Lanczos approach as coded in the program Quantum Espresso.[74,75] The charge density responses were visualized using the software VESTA version 3.5.7.[76]

Data availability

Data are available in the ESI.†

Conflicts of interest

Rice University owns the intellectual property rights on the use of MJHs for permeabilization of cell membranes. That intellectual property is currently unlicensed. Therefore, all authors declare no potential conflicts.

Acknowledgements

Funding was provided by The Discovery Institute and The Welch Foundation (C-2017-20220330). J. M. S. acknowledges funding from the Lannater and Herb Fox Professorship and the advanced computing resources provided at Texas A&M High Performance Research Computing (HPRC). We are thankful to Prof H. Xiao at Rice University for kindly hosting C. A. O. and sharing his laboratory to culture the A375 cancer cells. We thank Dr D. K. James for editing the manuscript. We also thank Dr A. B. Utama for confocal microscopy training and Dr H. Deshmukh for flow cytometry training at the Rice Shared Equipment Authority.

References

1 E. Prodan, C. Radloff, N. J. Halas and P. Nordlander, *Science*, 2003, **302**, 419–422.
2 E. Ozbay, *Science*, 2006, **311**, 189–193.
3 H. A. Atwater and A. Polman, *Nat. Mater.*, 2010, **9**, 205–213.
4 J. Langer, D. J. de Aberasturi, J. Aizpurua, R. A. Alvarez-Puebla, B. Auguié, J. J. Baumberg, G. C. Bazan, S. E. J. Bell, A. Boisen, A. G. Brolo, J. Choo, D. Cialla-May, V. Deckert, L. Fabris, K. Faulds, F. Javier García de Abajo, R. Goodacre, D. Graham, A. J. Haes, C. L. Haynes, C. Huck, T. Itoh, M. Käll, J. Kneipp, N. A. Kotov, H. Kuang, E. C. Le Ru, H. K. Lee, J. F. Li, X. Y. Ling, S. A. Maier, T. Mayerhöfer, M. Moskovits, K. Murakoshi, J. M. Nam, S. Nie, Y. Ozaki, I. Pastoriza-Santos, J. Perez-Juste, J. Popp, A. Pucci, S. Reich, B. Ren, G. C. Schatz, T. Shegai, S. Schlücker, L. L. Tay, K. George Thomas, Z. Q. Tian, R. P. van Duyne, T. Vo-Dinh, Y. Wang, K. A. Willets, C. Xu, H. Xu, Y. Xu, Y. S. Yamamoto, B. Zhao and L. M. Liz-Marzán, *ACS Nano*, 2020, **14**, 28–117.
5 B. Sharma, R. R. Frontiera, A. I. Henry, E. Ringe and R. P. Van Duyne, *Mater. Today*, 2012, **15**, 16–25.
6 N. Liu, M. Mesch, T. Weiss, M. Hentschel and H. Giessen, *Nano Lett.*, 2010, **10**, 2342–2348.
7 J. N. Anker, W. P. Hall, O. Lyandres, N. C. Shah, J. Zhao and R. P. Van Duyne, *Nat. Mater.*, 2008, **7**, 442–453.
8 K. C. Bantz, A. F. Meyer, N. J. Wittenberg, H. Im, Ö. Kurtulus, S. H. Lee, N. C. Lindquist, S. H. Oh and C. L. Haynes, *Phys. Chem. Chem. Phys.*, 2011, **13**, 11551–11567.
9 R. Bardhan, S. Lal, A. Joshi and N. J. Halas, *Acc. Chem. Res.*, 2011, **44**, 936–946.
10 O. Neumann, A. S. Urban, J. Day, S. Lal, P. Nordlander and N. J. Halas, *ACS Nano*, 2013, **7**, 42–49.
11 J. G. Smith, J. A. Faucheaux and P. K. Jain, *Nano Today*, 2015, **10**, 67–80.
12 L. Zhou, Y. Tan, J. Wang, W. Xu, Y. Yuan, W. Cai, S. Zhu and J. Zhu, *Nat. Photonics*, 2016, **10**, 393–398.
13 S. Linic, P. Christopher and D. B. Ingram, *Nat. Mater.*, 2011, **10**, 911–921.
14 Z. Zheng, W. Xie, B. Huang and Y. Dai, *Chem. - Eur. J.*, 2018, **24**, 18322–18333.
15 W. A. Murray and W. L. Barnes, *Adv. Mater.*, 2007, **19**, 3771–3782.
16 N. J. Halas, S. Lal, S. Link, W. S. Chang, D. Natelson, J. H. Hafner and P. Nordlander, *Adv. Mater.*, 2012, **24**, 4842–4877.
17 G. V. Naik, V. M. Shalaev and A. Boltasseva, *Adv. Mater.*, 2013, **25**, 3264–3294.
18 A. Manjavacas, F. Marchesin, S. Thongrattanasiri, P. Koval, P. Nordlander, D. Sánchez-Portal and F. J. García De Abajo, *ACS Nano*, 2013, **7**, 3635–3643.
19 A. Lauchner, A. E. Schlather, A. Manjavacas, Y. Cui, M. J. McClain, G. J. Stec, F. J. García De Abajo, P. Nordlander and N. J. Halas, *Nano Lett.*, 2015, **15**, 6208–6214.
20 Y. Cui, A. Lauchner, A. Manjavacas, F. J. García De Abajo, N. J. Halas and P. Nordlander, *Nano Lett.*, 2016, **16**, 6390–6395.
21 S. Bernadotte, F. Evers and C. R. Jacob, *J. Phys. Chem. C*, 2013, **117**, 1863–1878.
22 S. Gil-Guerrero, A. Pena-Gallego and M. Mandado, *J. Phys. Chem. C*, 2020, **124**, 1585–1593.
23 C. Ayala-Orozco, D. Galvez-Aranda, A. Corona, J. M. Seminario, R. Rangel, J. N. Myers and J. M. Tour, *Nat. Chem.*, 2024, **16**, 456–465.
24 C. Ayala-Orozco, B. Li, G. Li and J. M. Tour, *Chem. Sci.*, 2025, **16**, 2718–2729.
25 Z. Wang, A. Pakoulev and D. D. Dlott, *Science*, 2002, **296**, 2201–2203.
26 A. Tokmakoff, B. Sauter and M. D. Fayer, *J. Chem. Phys.*, 1994, **100**, 9035–9043.
27 V. M. Kenkre, A. Tokmakoff and M. D. Fayer, *J. Chem. Phys.*, 1994, **101**, 10618–10629.
28 W. Chen, P. Roelli, H. Hu, S. Verlekar, S. P. Amirtharaj, A. I. Barreda, T. J. Kippenberg, M. Kovylina, E. Verhagen, A. Martínez and C. Galland, *Science*, 2021, **374**, 1264–1267.

29 A. Xomalis, X. Zheng, R. Chikkaraddy, Z. Koczor-Benda, E. Miele, E. Rosta, G. A. E. Vandenbosch, A. Martínez and J. J. Baumberg, *Science*, 2021, **374**, 1268–1271.
30 C. Ayala-Orozco, C. Urban, M. W. Knight, A. S. Urban, O. Neumann, S. W. Bishnoi, S. Mukherjee, A. M. Goodman, H. Charron, T. Mitchell, M. Shea, R. Roy, S. Nanda, R. Schiff, N. J. Halas and A. Joshi, *ACS Nano*, 2014, **8**, 6372–6381.
31 C. Ayala-Orozco, G. Li, B. Li, V. Vardanyan, A. B. Kolomeisky and J. M. Tour, *Adv. Mater.*, 2024, **36**, 2309910.
32 S. Kara, S. Afonin, O. Babii, A. N. Tkachenko, I. V. Komarov and A. S. Ulrich, *Biochim. Biophys. Acta, Biomembr.*, 2017, **1859**, 1828–1837.
33 W. R. Redwood, F. R. Pfeiffer, J. A. Weisbach and T. E. Thompson, *Biochim. Biophys. Acta, Biomembr.*, 1971, **233**, 1–6.
34 H. Lindsey, N. O. Petersen and S. I. Chan, *Biochim. Biophys. Acta, Biomembr.*, 1979, **555**, 147–167.
35 K. A. Riske, T. P. Sudbrack, N. L. Archilha, A. F. Uchoa, A. P. Schroder, C. M. Marques, M. S. Baptista and R. Itri, *Biophys. J.*, 2009, **97**, 1362–1370.
36 R. Itri, H. C. Junqueira, O. Mertins and M. S. Baptista, *Biophys. Rev.*, 2014, **6**, 47–61.
37 A. Bour, S. G. Kruglik, M. Chabanon, P. Rangamani, N. Puff and S. Bonneau, *Biophys. J.*, 2019, **116**, 910–920.
38 A. M. Baxter and N. J. Wittenberg, *Langmuir*, 2019, **35**, 11542–11549.
39 A. Sakaya, I. O. L. Bacellar, J. L. Fonseca, A. M. Durantini, J. McCain, L. Xu, M. Vignoni, A. H. Thomas, M. S. Baptista and G. Cosa, *Langmuir*, 2023, **39**, 442–452.
40 M. N. Holme, I. A. Fedotenko, D. Abegg, J. Althaus, L. Babel, F. Favarger, R. Reiter, R. Tanasescu, P.-L. Zaffalon, A. Ziegler, B. Müller, T. Saxer and A. Zumbuehl, *Nat. Nanotechnol.*, 2012, **7**, 536–543.
41 O. Rifaie-Graham, N. F. B. Galensowske, C. Dean, J. Pollard, S. Balog, M. G. Gouveia, M. Chami, A. Vian, E. Amstad, M. Lattuada and N. Bruns, *Angew. Chem., Int. Ed.*, 2021, **60**, 904–909.
42 O. Lem, P. Gangurde, A. Koivuniemi, A. Keskinen, A. Efimov, N. Durandin and T. Laaksonen, *Carbohydr. Polym.*, 2024, **336**, 122134.
43 O. Rifaie-Graham, S. Ulrich, N. F. B. Galensowske, S. Balog, M. Chami, D. Rentsch, J. R. Hemmer, J. Read de Alaniz, L. F. Boesel and N. Bruns, *J. Am. Chem. Soc.*, 2018, **140**, 8027–8036.
44 R. Xiong, S. K. Samal, J. Demeester, A. G. Skirtach, S. C. De Smedt and K. Braeckmans, *Adv. Phys.:X*, 2016, **1**, 596–620.
45 T. Shigematsu, K. Koshiyama and S. Wada, *Sci. Rep.*, 2015, **5**, 15369.
46 K. Olbrich, W. Rawicz, D. Needham and E. Evans, *Biophys. J.*, 2000, **79**, 321–327.
47 T. Portet and R. Dimova, *Biophys. J.*, 2010, **99**, 3264–3273.
48 R. P. Rand, *Biophys. J.*, 1964, **4**, 303–316.
49 B. L. Mui, P. R. Cullis, E. A. Evans and T. D. Madden, *Biophys. J.*, 1993, **64**, 443–453.
50 F. Schneider, D. Ruhlandt, I. Gregor, J. Enderlein and A. I. Chizhik, *J. Phys. Chem. Lett.*, 2017, **8**, 1472–1475.
51 B. D. Knapp and K. C. Huang, *Annu. Rev. Biophys.*, 2022, **51**, 499–526.
52 Y. Bin Yan, Q. Wang, H. W. He and H. M. Zhou, *Biophys. J.*, 2004, **86**, 1682–1690.
53 Y. Reissis, E. García-Gareta, M. Korda, G. W. Blunn and J. Hua, *Stem Cell Res. Ther.*, 2013, **4**, 1–11.
54 Y. Zhang, X. Zhan, J. Xiong, S. Peng, W. Huang, R. Joshi, Y. Cai, Y. Liu, R. Li, K. Yuan, N. Zhou and W. Min, *Sci. Rep.*, 2018, **8**, 8720.
55 B. Leber, U. Mayrhauser, B. Leopold, S. Koestenbauer, K. Tscheliessnigg, V. Stadlbauer and P. Stiegler, *Anticancer Res.*, 2012, **32**, 915–921.
56 C. Shirata, J. Kaneko, Y. Inagaki, T. Kokudo, M. Sato, S. Kiritani, N. Akamatsu, J. Arita, Y. Sakamoto, K. Hasegawa and N. Kokudo, *Sci. Rep.*, 2017, **7**, 1–8.
57 J. Yu, D. Javier, M. A. Yaseen, N. Nitin, R. Richards-Kortum, B. Anvari and M. S. Wong, *J. Am. Chem. Soc.*, 2010, **132**, 1929–1938.
58 S. Chen, L. Zhu, Z. Du, R. Ma, T. Yan, G. Alimu, X. Zhang, N. Alifu and C. Ma, *RSC Adv.*, 2021, **11**, 20850–20858.
59 V. Houot, P. Etienne, A. Petitot, S. Barbier, J. Blein and L. Suty, *J. Exp. Bot.*, 2001, **52**, 1721–1730.
60 E. R. Whittemore, D. T. Loo and C. W. Cotman, *Neuroreport*, 1994, **5**, 1485–1488.
61 A. Weinberger, F. C. Tsai, G. H. Koenderink, T. F. Schmidt, R. Itri, W. Meier, T. Schmatko, A. Schröder and C. Marques, *Biophys. J.*, 2013, **105**, 154–164.
62 A. M. Firsov, J. Pfeffermann, A. S. Benditkis, T. I. Rokitskaya, A. S. Kozlov, E. A. Kotova, A. A. Krasnovsky, P. Pohl and Y. N. Antonenko, *J. Photochem. Photobiol., B*, 2023, **239**, 112633.
63 J. C. Phillips, D. J. Hardy, J. D. C. Maia, J. E. Stone, J. V. Ribeiro, R. C. Bernardi, R. Buch, G. Fiorin, J. Hénin, W. Jiang, R. McGreevy, M. C. R. Melo, B. K. Radak, R. D. Skeel, A. Singharoy, Y. Wang, B. Roux, A. Aksimentiev, Z. Luthey-Schulten, L. V. Kale, K. Schulten, C. Chipot and E. Tajkhorshid, *J. Chem. Phys.*, 2020, **153**, 044130.
64 J. Lee, X. Cheng, J. M. Swails, M. S. Yeom, P. K. Eastman, J. A. Lemkul, S. Wei, J. Buckner, J. C. Jeong, Y. Qi, S. Jo, V. S. Pande, D. A. Case, C. L. Brooks, A. D. MacKerell, J. B. Klauda and W. Im, *J. Chem. Theory Comput.*, 2016, **12**, 405–413.
65 B. R. Brooks, C. L. Brooks, A. D. Mackerell, L. Nilsson, R. J. Petrella, B. Roux, Y. Won, G. Archontis, C. Bartels, S. Boresch, A. Caflisch, L. Caves, Q. Cui, A. R. Dinner, M. Feig, S. Fischer, J. Gao, M. Hodoscek, W. Im, K. Kuczera, T. Lazaridis, J. Ma, V. Ovchinnikov, E. Paci, R. W. Pastor, C. B. Post, J. Z. Pu, M. Schaefer, B. Tidor, R. M. Venable, H. L. Woodcock, X. Wu, W. Yang, D. M. York and M. Karplus, *J. Comput. Chem.*, 2009, **30**, 1545–1614.
66 J. Huang, S. Rauscher, G. Nawrocki, T. Ran, M. Feig, B. L. De Groot, H. Grubmüller and A. D. MacKerell, *Nat. Methods*, 2016, **14**, 71–73.
67 S. Jo, T. Kim, V. G. Iyer and W. Im, *J. Comput. Chem.*, 2008, **29**, 1859–1865.

68 S. Kim, J. Lee, S. Jo, C. L. Brooks, H. S. Lee and W. Im, *J. Comput. Chem.*, 2017, **38**, 1879–1886.
69 F. Neese, F. Wennmohs, U. Becker and C. Riplinger, *J. Chem. Phys.*, 2020, **152**, 224108.
70 E. L. Wu, X. Cheng, S. Jo, H. Rui, K. C. Song, E. M. Dávila-Contreras, Y. Qi, J. Lee, V. Monje-Galvan, R. M. Venable, J. B. Klauda and W. Im, *J. Comput. Chem.*, 2014, **35**, 1997–2004.
71 S. Jo, J. B. Lim, J. B. Klauda and W. Im, *Biophys. J.*, 2009, **97**, 50–58.
72 S. Jo, T. Kim and W. Im, *PLoS One*, 2007, **2**, e880.
73 J. Lee, D. S. Patel, J. Stahle, S. J. Park, N. R. Kern, S. Kim, J. Lee, X. Cheng, M. A. Valvano, O. Holst, Y. A. Knirel, Y. Qi, S. Jo, J. B. Klauda, G. Widmalm and W. Im, *J. Chem. Theory Comput.*, 2019, **15**, 775–786.
74 O. B. Malcıoğlu, R. Gebauer, D. Rocca and S. Baroni, *Comput. Phys. Commun.*, 2011, **182**, 1744–1754.
75 P. Giannozzi, S. Baroni, N. Bonini, M. Calandra, R. Car, C. Cavazzoni, D. Ceresoli, G. L. Chiarotti, M. Cococcioni, I. Dabo, A. Dal Corso, S. de Gironcoli, S. Fabris, G. Fratesi, R. Gebauer, U. Gerstmann, C. Gougoussis, A. Kokalj, M. Lazzeri, L. Martin-Samos, N. Marzari, F. Mauri, R. Mazzarello, S. Paolini, A. Pasquarello, L. Paulatto, C. Sbraccia, S. Scandolo, G. Sclauzero, A. P. Seitsonen, A. Smogunov, P. Umari and R. M. Wentzcovitch, *J. Phys. Condens. Matter*, 2009, **21**, 395502.
76 K. Momma and F. Izumi, *J. Appl. Crystallogr.*, 2011, **44**, 1272–1276.